Astronomy & Astrophysics manuscript no. S0_rotation
April 23, 2024

Strong-lensing and kinematic analysis of CASSOWARY 31: can strong lensing constrain the masses of multi-plane lenses?

H. Wang[1,2], R. Cañameras[1,2], S. H. Suyu[1,2,3], A. Galan[2,1], C. Grillo[4,5], G. B. Caminha[2,1], and L. Christensen[6]

[1] Max-Planck-Institut für Astrophysik, Karl-Schwarzschild-Str. 1, 85748 Garching, Germany
e-mail: wanghan@mpa-garching.mpg.de
[2] Technical University of Munich, TUM School of Natural Sciences, Physics Department, James-Franck Str. 1, 85748 Garching, Germany
[3] Academia Sinica Institute of Astronomy and Astrophysics (ASIAA), 11F of ASMAB, No. 1, Section 4, Roosevelt Road, Taipei 10617, Taiwan
[4] Dipartimento di Fisica, Università degli Studi di Milano, via Celoria 16, I-20133 Milano, Italy
[5] INAF-IASF Milano, via A. Corti 12, I-20133 Milano, Italy
[6] Cosmic Dawn Center, Niels Bohr Institute, Univ. of Copenhagen, Jagtvej 128, 2200 Copenhagen, Denmark

Received / Accepted

ABSTRACT

We present a mass measurement for the secondary lens along the line of sight (LoS) in the multi-plane strong lens modeling of the group-scale lens CASSOWARY 31 (CSWA 31). The secondary lens at redshift $z = 1.49$ is a spiral galaxy well aligned along the LoS with the main lens at $z = 0.683$. Using the MUSE integral-field spectroscopy of this spiral galaxy, we measure its rotation velocities and determine the mass from the gas kinematics. We compare the mass estimation of the secondary lens from the lensing models to the mass measurement from kinematics, finding that the predictions from strong lensing tend to be higher. By introducing an additional lens plane at $z = 1.36$ for an overdensity known to be present, we find a mass of $\simeq 10^{10}$ $M_\odot$ enclosed within 3.3 kpc from the centroid of the spiral galaxy, approaching the estimate from kinematics. This shows that secondary-lens mass measurements from multiple-plane modeling are affected by systematic uncertainties from the degeneracies between lens planes and the complex LoS structure. Conducting a detailed analysis of the LoS structures is therefore essential to improve the mass measurement of the secondary lens.

Key words. gravitational lensing: strong – data analysis: methods

1. Introduction

In the ΛCDM model, galaxies grow hierarchically by accretion of cold gas from the circumgalactic medium and by mergers with nearby galaxies. Measuring robust galaxy masses over broad redshift ranges is key to improving our understanding of this broad picture (e.g., Peng et al. 2010). Yet, at high redshifts ($z \geq 1$), direct measurements are challenging due to observational limitations, and mass estimates not only rely on assumptions derived from our knowledge of the nearby Universe, but are also prone to several systematics. For instance, for gas-rich spiral galaxies, dynamical masses inferred from gas kinematics can be significantly biased in case of departures from smooth rotation due to secular instabilities (e.g., Yu et al. 2022), merging events, or feedback processes (e.g., Soto et al. 2012).

In that context, strong lensing has been established as a robust, accurate tracer of the total mass and inner structure of foreground galaxies (e.g., Koopmans et al. 2006; Auger et al. 2010; Shajib et al. 2022), galaxy groups and clusters (e.g., Treu 2010; Meneghetti et al. 2017). Photons travelling from distant sources get deflected by an over-dense region associated with the foreground galaxies and form arcs or a full Einstein ring around the deflectors. The locations of the lensed images and the surface brightness of the extended arcs can be used to constrain the mass distribution of the foreground deflectors.

In most strong lensing scenarios, a single over-dense region along the path between the source and observer is considered for modeling. The line-of-sight (LoS) structure is neglected, which is usually a sensible approximation since the main lens contributes dominantly to the deflection angle (e.g., Gavazzi et al. 2008). In some cases, galaxies aligned with the main lens can nonetheless produce non-negligible perturbations, particularly for group- and cluster-scale lenses, which tend to have rich LoS structures (Bayliss et al. 2014). To reconstruct the lensed sources and improve the root mean square (rms) of the predicted image position for such systems, a secondary lens needs to be included in computing multiple-lens-plane models (e.g., Schneider 2014; Wong et al. 2017).

In this work, we further explore the constraints on the mass of secondary lenses inferred from multi-plane lens models by conducting a case study based on the group-scale lens CASSOWARY 31 (CSWA 31, Belokurov et al. 2009; Stark et al. 2013). In Wang et al. (2022), through detailed modeling of the multi-scale mass distribution, we found that this system comprises a spiral galaxy at $z = 1.49$ well-aligned with the main lens at $z = 0.683$, with both structures contributing significantly to the deflection angles of source galaxies at higher redshifts. In addition to strong lensing, gas kinematics inferred from integral-field spectroscopy (IFS) with the Multi-Unit Spectroscopic Explorer allow us to infer an independent mass estimate for this secondary lens. While the population of such systems with two or more deflectors is rare, their number is expected to increase with the next generation of deep, wide-field imaging surveys such as the Legacy Survey of Space and Time, Euclid, and Roman (e.g., Collett 2015; Mandelbaum et al. 2018). It is therefore becom-

ing essential to investigate the ability of multi-plane lens modeling as an alternative mass probe to study the inner structure of galaxies acting as secondary deflectors.

The paper is organized as follows. In Sect. 2, we briefly introduce the properties of CSWA 31 and the data sets. In Sect. 3, we present the independent mass measurements from strong lensing and kinematic modeling. In Sect. 4, we discuss the uncertainties of each method and compare the results. We also present an updated model with an additional lens plane. In Sect. 5, we summarise our findings and discuss the validity of mass predictions for secondary lenses obtained from multi-plane lens modeling. Throughout this work we assume $H_0 = 70\,\mathrm{km\ s^{-1}\ Mpc^{-1}}$, $\Omega_\mathrm{m} = 0.3$, and $\Omega_\Lambda = 0.7$. Hence, $1''$ corresponds to 7.08 kpc at the main lens redshift of $z = 0.683$, and to 8.46 kpc at the secondary lens redshift of $z = 1.49$.

2. Data

CSWA 31 is a group-scale lens with a central ultra-massive brightest group galaxy (BGG) at $z = 0.683$, surrounded by six sets of multiple images from five independent background sources. The high-resolution HST imaging in F160W and F438W filters, the VLT/MUSE spectroscopy of the field (program 0104.A-0830(A), PI: Cañameras), and the joint analysis of these data are described in detail in Wang et al. (2022). The background spiral galaxy at $z = 1.49$ studied in this letter and referred to as S0, is lensed into four multiple images forming an extended arc (see Fig. 1). We identified five additional sets of multiple images S1, S2, S3, S4 and S5 at four independent redshifts, using MUSE spectroscopic and HST (F160W−F438W) colors. Image sets S1 and S2 are at redshift $z = 1.49$ and S3, S4 and S5 at redshifts $z = 2.76$, 3.43 and $z = 4.21$ respectively. In addition, 46 group members located within ± 3000 km s^{-1} from the BGG redshift were selected from the MUSE spectroscopic catalog.

The spiral galaxy S0 displays a disk-like morphology in HST/F160W, with a bright bulge and three main spiral arms, and is apparently oriented nearly face-on. The best-fit Sérsic profile of image S0(d) shows that this galaxy has an effective radius R_eff of $1.17''$, or about 3.8 kpc in the source plane (after correcting for magnification), and an axis ratio $q = 0.85$. The properties of S0 are similar to the strongly lensed spiral galaxy at $z \approx 1.5$ hosting SN Refsdal, for which Di Teodoro et al. (2018) inferred 3D kinematic models.

In this work, we focus on the least distorted image S0(d), shown in Fig. 1 left inset, to conduct a kinematic analysis of S0 in the image plane (see also Di Teodoro et al. 2018). We verify that spatial variations of lensing shear are negligible for S0(d) using the mass model Esr2−MP$_\mathrm{test}$ from Wang et al. (2022) (`baseline` model hereafter). We use this model to map small circles of $0.052''$ radius distributed over the source plane at $z = 1.49$, to the image S0(d). The circular sources get magnified and distorted into ellipses in the image plane, but these ellipses do not vary significantly in size and orientation over S0(d), suggesting overall uniform lensing distortions over this image (see the green ellipses on the inset of Fig. 1 left panel). In addition, the magnification factor $\mu \simeq 7$ of image S0(d) offers a good opportunity to zoom-in onto the gas kinematics of this spiral.

The MUSE data cube has a Point Spread Function (PSF) with a full width at half maximum (FWHM) of $0.75'' \times 0.73''$. Its wavelength resolution is FWHM = 2.35 Å, with a channel width of 1.25 Å. To focus on the [OII] doublet, the cube was cropped between 3719 Å to 3734 Å in the rest frame of S0. The [OII] line intensity map of S0(d) shows an asymmetrical feature, indicating that ionized gas reservoirs form denser regions along the spiral arms seen in stellar continuum with HST (see Fig. 1). The total [OII] flux over the source is 203.8×10^{-18} erg s^{-1}. The line-of-sight velocity map is derived by fitting double Gaussian functions to each pixel, representing a preliminary step to investigate the presence of velocity gradients within the S0(d) image. Additionally, these maps offer initial values for geometrical parameters in ^{3D}`Barolo`.

3. Methodology

To investigate the constraints on secondary lens masses, we infer two independent mass estimates of the S0 spiral. In Sect. 3.1, we present the kinematic modeling procedure and the mass measurement from the best-fit rotation curve. In Sect. 3.2, we present the multi-plane strong lens modeling and the S0 mass measurement from the lensing approach.

3.1. Mass measurement from kinematic modeling

Spiral galaxies at $z \geq 1$ are thought to settle into marginally stable, rotating disks with turbulence (e.g., Bournaud et al. 2009; Nestor Shachar et al. 2023). The apparent velocity gradient in Fig. 1 and the smooth disk-like morphology from HST suggest a rotating velocity field. We adopt ^{3D}`Barolo` (Di Teodoro & Fraternali 2015) to derive a simple rotating disk model of S0 using the MUSE data of image S0(d), following a similar approach as Di Teodoro et al. (2018). This image is well deblended from other galaxies in the field and the minor distortions of S0(d) caused by strong lensing vary on scales smaller than the MUSE PSF. The beam-smearing of galaxy kinematics, which is accounted for by ^{3D}`Barolo`, dominates over systematic errors due to lensing shear.

^{3D}`Barolo` initially identifies a mask region within the MUSE data cube encompassing the emission lines. Subsequently, it builds a kinematic model convolved with the MUSE PSF to characterize these lines by using tilted rings. In our case, ^{3D}`Barolo` replicates the [OII] emission doublet at $\lambda = 3726$ Å and 3729 Å. Each ring is defined with a centroid, position angle, inclination angle i, systematic velocity V_sys, rotation velocity V_rot and velocity dispersion σ_v. We build the kinematic model by using four tilted rings, with a $0.4''$ width, and adopting the S0(d) centroid in HST imaging with the S0 position angle determined from the velocity gradient (see Fig. 1) as initial values. We fix the V_sys in all tilted rings to 0 km s^{-1}. We iteratively refine these values with ^{3D}`Barolo`, and subsequently allow variations in only the V_rot and σ_v at each ring (see Fig. A.1). In the fitting, we adopt the `local` normalization and a uniform weighting function[3] to account for the asymmetry in the intensity map of S0(d).

^{3D}`Barolo` projects the tilted ring model to the plane of the sky using i and compares it to the observational data. The inclination angle is an important parameter, but it is hard to estimate in practice due to the unknown intrinsic shape of galaxies. Without losing any generality, we build a range of kinematic models covering i from 5° to 35° (see discussion in Sect. 4.1). The inclination is not well constrained, and Fig. 2 shows a typical best-fit model per wavelength channel, for $i = 20.8°$.

Due to the moderate spectral resolution of the MUSE data cube, velocity dispersion values returned by ^{3D}`Barolo` decrease to 0 km s^{-1} for the inner radius of $0.2''$ and the outer radius of $1.4''$, for all kinematic models with inclination angles between

[3] For the "type-two" residual defined in Eqs. (2) and 3(b) in Sect. 2.4 of Di Teodoro & Fraternali (2015).

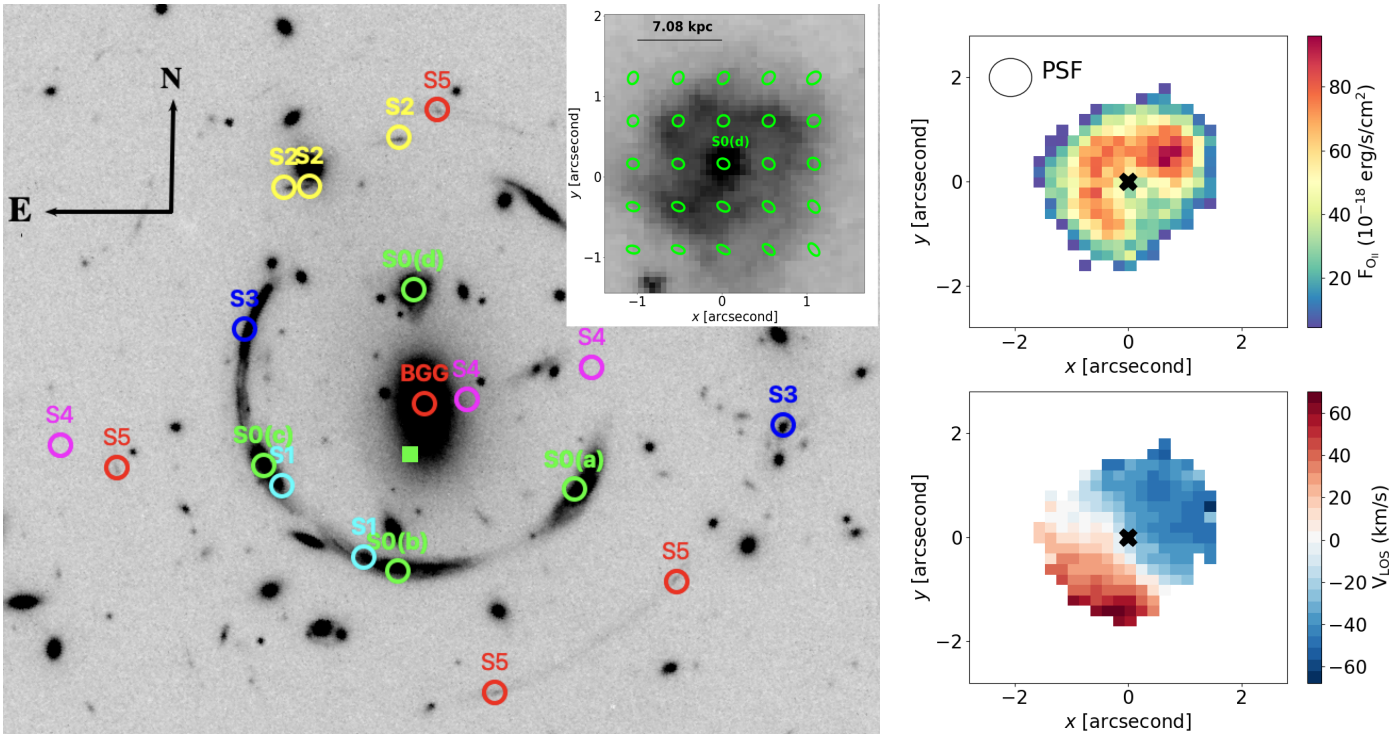

Fig. 1: *Left panel:* HST/WFC3 image of CSWA 31 in F160W band. The orientation is marked by the black arrows (north upward and east leftward) and kept fixed for other panels. The BGG at $z = 0.683$ is surrounded by 6 multiple-image sets at different redshifts marked with circles, using a different color for each set. The image sets S0 and S1 are bright features from the same spiral galaxy at $z = 1.49$, with a zoom-in image of S0(d) in the right inset. The green square shows the delensed S0 position in the HST imaging. The green ellipses in the zoom-in figure illustrate the minor variations in distortion over S0(d) caused by strong lensing. *Right panel:* The [OII] intensity map (top), and the LoS velocity map (bottom) for the S0(d) image were extracted from MUSE IFS. The FWHM of MUSE PSF is shown in the upper left in the intensity map. The bold black cross shows the adopted S0(d) centroid determined from `3DBarolo`.

5° and 35°. To address this limitation, we reduce the number of rings to three and obtain the best-fit σ_v at distances of 0.6″, 0.9″, and 1.2″ from the centroid of image S0(d), finding an average value of $\sigma_v = 41.3$ km s^{-1}. However, the residuals in the channel maps are worse than the model built with four rings (see Fig. A.2). We thus decide to retain the model with four rings and solely adopt the V_{rot} along the major axis at the second ring at $r = 0.6''$ and the third ring at $r = 1.0''$ to determine the dynamical mass of S0 (see Fig. 3).

We determine the total mass of S0 using V_{rot} via:

$$M_{rot}(r') = \frac{V_{rot}^2}{G} r', \quad (1)$$

where r' is the radial distance from the S0 centroid in the source plane at $z = 1.49$. Strong lensing magnifies a circular source with area $\pi r'^2$ by a factor of μ in the image plane (see Tab. 1). We convert the radii r in the S0(d) image to radii r' in the source plane via

$$r' = \frac{r}{\sqrt{\mu}} \quad (2)$$

We obtain a total mass of S0 of $\simeq 10^{10}$ $M_\odot$ at 3.3 kpc in the source plane, which is about the effective radius of S0 at $z = 1.49$ (see Fig. 4).

3.2. Mass measurement from multi-plane lens modeling

We summarize in Tab. 1 the different lens models we consider in this work. In this section, we adopt the multi-plane lens models Img−2MP, Img−2MP(L/D) and `baseline` from Wang et al. (2022). The average magnification factor μ of S0(d) has minor variations among these models, and the induced shear is negligible, as shown in Fig. 1 for the `baseline` model.

These three models consist of two lens planes, and were obtained with the `GLEE` software (Suyu & Halkola 2010; Suyu et al. 2012). The main lens plane at $z = 0.683$ accounts for the mass of BGG, group halo and group members. The secondary lens plane at $z = 1.49$ accounts for the mass of the spiral galaxy S0, which serves as a lensed source, being deflected by the main lens. Additionally, as a secondary lens along the line of sight, S0 deflects the light from the background sources S3, S4, and S5 at higher redshifts. Accounting for this secondary strong deflector (S0) improves the fitting of the image positions of S3, S4, and S5, while also enabling the simultaneous reconstruction of the extended sources S0 and S3 in the `baseline` model. Excluding the secondary lens plane in the modeling results in the failure to reconstruct S3 and leads to higher errors in the predicted image positions of S3, S4, and S5.

In all three models, S0 is modeled with a spherical isothermal (SIS) profile, which has a 3D density profile described as:

$$\rho(r) = \frac{{\sigma_v}^2}{2\pi G r^2}, \quad (3)$$

where σ_v is the velocity dispersion, related to the Einstein radius θ_E (for a lensed background source at infinite redshift) via ${\sigma_v}^2 =$

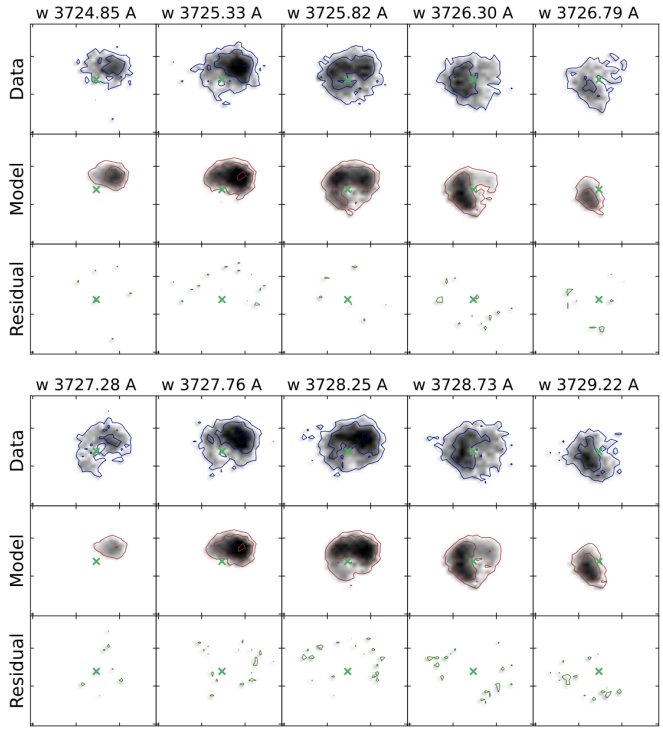

Fig. 2: Comparison between MUSE integral-field spectroscopy of image S0(d) (blue contours) and the ^{3D}`Barolo` model (red contours). The third row in the upper and bottom panels shows the residuals. Contour levels are set at $2\sigma n$, where the σ noise $= 2\times10^{-20}$ erg s^{-1} cm^{-2} Å^{-1} and $n = 1, 2, 4, 8$. The green cross shows the centroid position of S0(d). This plot shows the fitting result for the two lines of the [OII] emission doublet at (rest-frame) $\lambda = 3726$ Å and 3729 Å, in the upper and bottom panels, respectively.

$\frac{\theta_{\rm E}c^2}{4\pi}$. Thus, Eq. (3) can be written in terms of $\theta_{\rm E}$:

$$\rho(r) = \frac{\theta_{\rm E}c^2}{8\pi^2 G r^2}. \quad (4)$$

We calculate the mass of S0 enclosed within radius r' in spherical coordinates:

$$M_{\rm lens}(r') = \int_0^{r'} 4\pi r^2 \frac{\theta_{\rm E}c^2}{8\pi^2 G r^2}\, dr \quad (5)$$

such that,

$$M_{\rm lens}(r') = \frac{\theta_{\rm E}c^2}{2\pi G} r', \quad (6)$$

where r' is the radial distance in the source plane. Eq. (6) is valid in the inner region of the galaxy within the halo truncation.

The lens models Img−2MP, Img−2MP(L/D) and `baseline` adopted in this study rely on different sets of observational constraints to ascertain the best-fit values of the Einstein radius $\theta_{\rm E,S0}$ (see Tab. 1). The model Img−2MP adopts image positions of six multiple-image sets as constraints. In model Img−2MP(L/D), Wang et al. (2022) combines the stellar kinematics of the BGG with the multiple image positions, to perform a joint strong lensing and dynamical modeling. The `baseline` model uses extended arcs of S0 and S3 in addition to the image positions of three multiple-image sets S2, S4 and S5 as constraints. In Fig. 4, we plot the S0 mass distribution as a function of the source plane radius for these three models. The S0 mass predicted from the `baseline` model is three times smaller than that for the other two, and we further analyze this discrepancy in Sect. 4.2.

Table 1: Summary of the strong lens models used in this study, their different constraints, and the best-fit values of $\theta_{\rm E,S0}$.

Model name	Constraints	$\theta_{\rm E,S0}$	μ
Img−2MP	6 lensed-image sets	4.4″	5.5
Img−2MP (L/D)	6 sets + kinematics of BGG	4.6″	6.9
`baseline`	3 sets + extended arcs of S0, S3	1.65″	6.7
Esr2−3MP	3 sets + extended arcs of S0, S3	0.85″	7.3

Notes. The first three models share the same configuration and mass parametrization. In the last model Esr2-3MP, we account for the additional perturbation caused by foreground galaxies at $z = 1.36$ and perform lens modeling with three lens planes.

4. Mass comparison and discussion

Strong lens models presented in Sect. 3.2 tend to assign significantly more mass to S0 than the modeling of gas kinematics. We discuss this discrepancy by highlighting the main uncertainties from each approach in Sect. 4.1 and 4.2. In Sect. 4.2.1, we discuss the results from the two-plane lens models which are presented in Wang et al. (2022). Then, in Sect. 4.2.2, we present an additional model with a third lens plane to further explore the impact of LoS structures.

4.1. Uncertainties from the kinematic modeling

The unknown inclination angle i of the spiral has the largest contribution to the error budget on the mass inferred from kinematic modeling. Since S0 is observed nearly face-on, a small variation of i leads to significant changes in the rotation velocity along the major axis, as $V_{\rm rot} = V_{\rm LoS}/\sin i$. To obtain a sensible estimation of the uncertainty caused by i, we randomly draw 5000 samples from a broad range of angles i over [5°, 35°] and fit the MUSE data cube for each sample. We perform a model comparison by making use of the Bayesian Information Criterion (BIC). Since we use the same data cube and only allow the $V_{\rm rot}$ and $\sigma_{\rm v}$ to vary in each sample, the BIC in our case is computed by the log-likelihood term. We follow the approach of Birrer et al. (2019) defining the BIC weight w_i with respect to the minimal BIC value BIC$_{\rm min}$ in our sample,

$$w_i = \frac{\exp\{-({\rm BIC}_i - {\rm BIC}_{\rm min})/2\}}{\sum_{i=1}^{5000}\exp\{-({\rm BIC}_i - {\rm BIC}_{\rm min})/2\}}. \quad (7)$$

We then determine the median $V_{\rm rot}$ and the 1-σ uncertainty from the 16th, 50th and 84th of the weighted $V_{\rm rot}$ at radii of 0.6 ″ and 1.0 ″ (on the image plane) from the centroid of image S0(d), which correspond to 2.0 kpc and 3.3 kpc in the source plane (see Fig. 3).

We obtain the median values of $V_{\rm rot} = 123$ km s^{-1} and $\sigma_{\rm v} = 40$ km s^{-1} at 3.3 kpc from the galaxy center, and a ratio $V_{\rm rot}/\sigma_{\rm v}$ of 3.1 showing that this spiral galaxy is indeed rotationally-supported. Median values are broadly consistent with the evolution of ionized gas kinematics of star-forming galaxies at $z \approx 1$–2 in the literature (e.g., Wisnioski et al. 2015; Übler et al. 2019; Genzel et al. 2020; Price et al. 2021; Puglisi et al. 2023). With a similar modeling of the [OII] doublet, Di Teodoro et al. (2018)

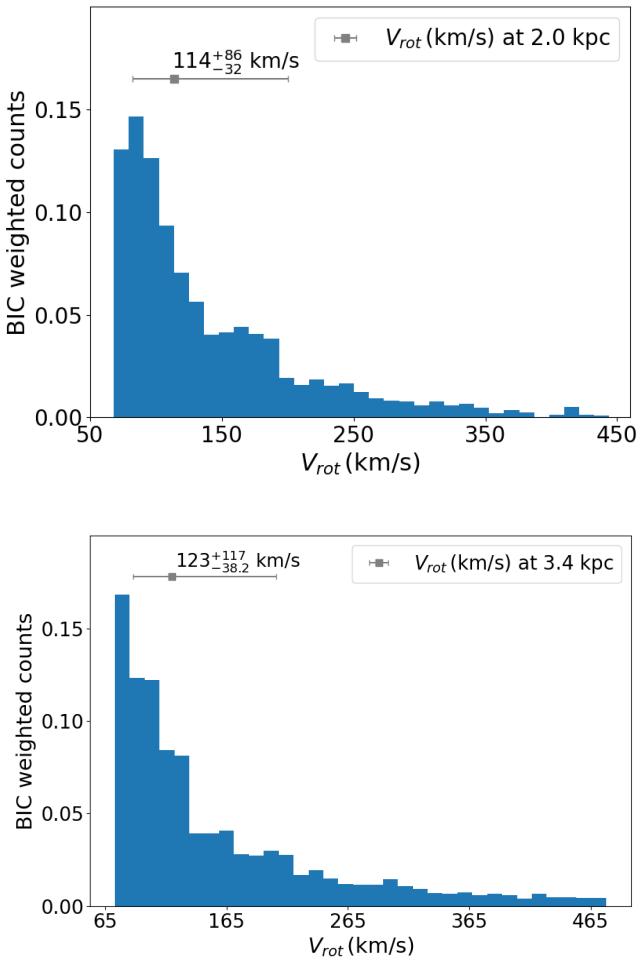

Fig. 3: The histogram of $V_{\rm rot}$ weighted by BIC. The upper and bottom panels show the weighted $V_{\rm rot}$ distribution at 2.0 kpc and at 3.3 kpc from the galaxy centroid in the source plane, respectively. The 1-σ uncertainties on $V_{\rm rot}$ are determined by drawing 5000 samples of the inclination angles in the range [5°, 35°].

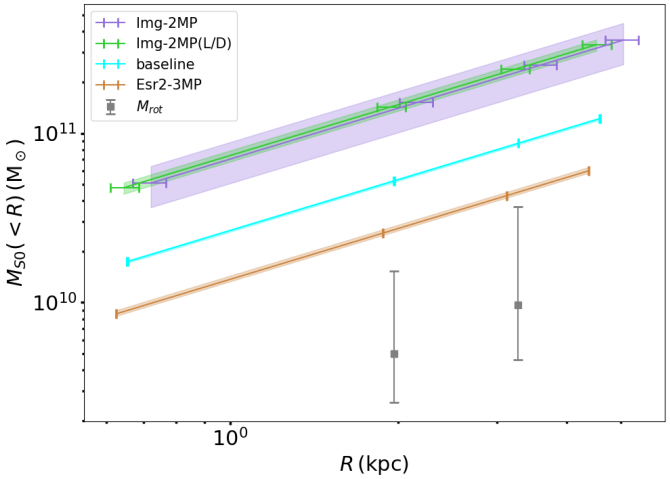

Fig. 4: Comparison of mass distributions for the spiral galaxy S0 at source plane from strong lensing and kinematic modeling. The solid lines show the S0 mass estimated from lens models using Eq. (6), given different data sets as constraints (see Tab. 1). The statistical 1-σ uncertainty of S0 mass from lens models is estimated from the 16th, 50th and 84th percentiles of the posterior probability distribution functions (PDFs). The 1-σ uncertainty along the x-axis of the S0 mass is from the magnification modification using Eq. (2). The grey squares show the S0 mass estimated from kinematic modeling using Eq. (1). The radial distance of the grey squares is divided by μ from the `baseline` model. The error bar shows 1-σ uncertainties associated with the range of inclination angles.

characterized the kinematics of the spiral hosting SN Refsdal up to 8 kpc from the galaxy center, probing into the flat portion of the rotation curve. While their similar $V_{\rm rot}$ and lower $\sigma_{\rm v} \simeq 27$ km s^{-1} indicate stronger rotation support, the properties of both spirals at $z \approx 1.5$ are broadly consistent.

We use the value of $V_{\rm rot}$ at 3.3 kpc to place S0 on the stellar-mass Tully-Fisher relation (TFR). We obtain an estimate of the galaxy stellar mass by fitting the g-, r-, i-, z-band photometry of image S0(d) from the DESI Legacy Surveys DR10, together with the F160W band from HST with CIGALE (Boquien et al. 2019), and following the approach described in Wang et al. (2022). This yields $M_* = (2.1 \pm 0.4) \times 10^{10}$ M$_\odot$, corrected by $\mu = 6.7$ from the `baseline` model, showing that S0 follows the stellar-mass TFR at $z \simeq 0$ from McGaugh & Schombert (2015) (see Fig. A.3). The stellar mass is also comparable to the total mass at $R_{\rm eff}$ from the kinematic analysis, showing that the baryonic component dominates the inner mass budget.

Moreover, we test the impact of the mask region detected by $^{\rm 3D}$`Barolo` on the fitting results. We use different detection modes and noise thresholds to infer the mask region and to reproduce the fitting. The resulting variations in output velocities are minor and within the 1-σ range above.

As stated in Sect. 3.1, we neglect the effect of pressure support to the modeling, assuming that the gas kinematics of S0 follow perfect circular motions. The low intrinsic velocity dispersion suggests that the ionized gas in S0 is relatively less turbulent than in other disks at $z \gtrsim 1$ (e.g., Swinbank et al. 2011), and asymmetric drift corrections due to pressure support should only have minor impact on the measured $V_{\rm rot}$. Other feedback processes could also produce radial motions for the stellar and gas components in S0. In particular, large-scale outflowing winds are a common property for star-forming galaxies at $z \gtrsim 1$ (e.g., Newman et al. 2012; Bradshaw et al. 2013), and can influence their internal mass distributions. However, converting the [OII] flux of image S0(d) to a star formation rate, using the Kennicutt (1998) relation and a Salpeter (1955) initial mass function, would place S0 near, or even slightly below the star formation main sequence at $z \approx 1.5$ (e.g., Popesso et al. 2023). In consequence, while error bars shown in Fig. 4 might be broadened by such feedback effects, they are unlikely to play a significant role on the dynamical mass measurement of S0.

4.2. Uncertainties from strong lens modeling

The uncertainties in the S0 mass measurement through the lensing approach arise from degeneracies between the primary and secondary lens planes, as well as from LoS effects.

4.2.1. Two-lens-plane modeling

The mass distribution of S0 from the two-plane lens models described in Sect. 3.2 can be classified into two groups. Firstly, the model Img−2MP based on image positions and the model Img−2MP (L/D) combining with the BGG stellar kinematics both predict an elevated mass of $\simeq 10^{11}\,M_\odot$ at 3.3 kpc. This falls on the high-mass end of the RC41 sample at $z \simeq 0.65$–2.45 from Genzel et al. (2017). Secondly, the `baseline` model using image positions and the extended arcs as constraints predicts a lower $\theta_{E,S0}$ of 1.65″. Because the mass degeneracies between the main lens plane at $z = 0.683$, and S0 at $z = 1.49$, are partially broken by the additional constraints from extended arcs, $\theta_{E,S0}$ decreases from $\simeq 4''$to 1.65″.

To further probe this difference, we check the impact of changing the prior on $\theta_{E,S0}$, from the broad flat prior between 0″ and 5″assumed in the `baseline` model, to an informative prior motivated by the kinematic analysis. Assuming that the S0 mass from dynamical and lens modeling are identical, we obtain

$$\theta_E = \frac{2\pi}{c^2} V_{rot}^2. \quad (8)$$

In that case, the best-fit $\theta_{E,S0}$ in the `baseline` model corresponds to a constant V_{rot} of 338.3 km s^{-1} as a function of radius, a value above the 1-σ upper limit from `3DBarolo` (see Fig. 3). On the other hand, the median rotation velocities correspond to $\theta_E \simeq 0.2''$. We assign a Gaussian prior $\mathcal{G}$ (0.2″, 0.07″) to $\theta_{E,S0}$ and recomputed the `baseline` model. The best-fit $\theta_{E,S0}$ only decreases mildly to 1.62″.

Consequently, parameter degeneracies cannot entirely explain the tension between the two modeling approaches. Since the S0 mass is also affected by the choice of the mass parameterisation, we also model S0 with the elliptical power law and dPIE profiles, finding that the resulting S0 mass remains similar to that of the `baseline`. We thus consider that some additional sources along the line-of-sight discarded from the model might be projected onto the mass plane at $z = 1.49$ and artificially boosting the S0 mass estimate.

4.2.2. Three-lens-plane modeling

To further investigate the impact of LoS effects on the S0 mass measurement from strong lensing, we build a model with a third lens plane at $z = 1.36$. Using the MUSE redshift catalogue from Wang et al. (2022), we find 21 galaxies at $z = 0.7$–0.85 and seven at $z = 1.36$. Two galaxies at $z = 1.36$ are within 15″ from the BGG centroid and have F160W < 22 mag, while none of the galaxies at $z = 0.7$–0.85 reach F160W < 22 mag within this aperture. Together with the distance to the extended arcs, this suggests that galaxies at $z = 1.36$ are stronger LoS perturbers. We assign an SIS profile at $z = 1.36$ and perform the lens modeling with three planes at $z = 0.683$ (main lens plane), $z = 1.36$ (perturbers), and $z = 1.49$ (S0), adopting the same constraints as in the `baseline` model. The best-fit model results in $\theta_{E,S0} = 0.85''$ and $\theta_{E,z=1.36} = 0.59''$ (Einstein radius of perturbers at $z = 1.36$).

The enclosed mass of S0 within 3.3 kpc from this new model (Esr2−3MP, see Tab. 1) is close to the 68% percentile from the kinematic measurement (see the brown line in Fig. 4). We project the observed image positions of S0 at $z = 0.683$ onto the newly added lens plane at $z = 1.36$, finding that the projected images of S0 are close to the best-fit perturber position (see Fig. 5). The closer the perturber at $z = 1.36$ is to the projected S0 image positions, the greater its best-fit mass. When the perturber moves away from the projected S0 image positions, the value of

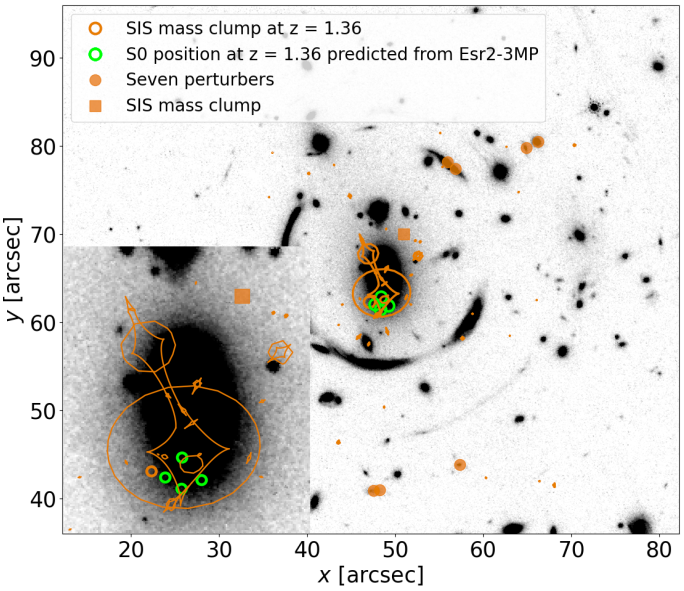

Fig. 5: The positions of the seven perturbers at $z = 1.36$ (filled brown circles) and the caustics at $z = 1.36$ based from model Esr2−3MP (brown dashed lines). Offsets are relative to the coordinate origin at the bottom-left corner of the HST/F160W image. The filled brown square shows the centroid of the SIS mass profile in model Esr2-3MP. The solid brown and green circles show the centroid of the SIS mass profile and the lensed source S0 projected onto the lens plane at $z = 1.36$, respectively. The position of the SIS at $z = 1.36$ is close to one of the projected S0 images, showing that this perturber affects the light propagation of S0 along the LoS.

$\theta_{E,S0}$ falls back to that of the `baseline` model. In the Esr2−3MP model, we assign broad flat priors in the range [0″, 5″] for $\theta_{E,S0}$ and $\theta_{E,z=1.36}$, and obtain strong degeneracies between the mass profiles in the three lens planes (see Fig. B.1). $\theta_{E,S0}$ is negatively correlated with the Einstein radius of the group-halo $\theta_{E,GH}$ and with $\theta_{E,z=1.36}$, and is positively correlated with the Einstein radius of the BGG $\theta_{E,BGG}$.

Our model Esr2−3MP provides comparable fitting results as `baseline`. It improves the modeling of extended arcs for S0 and S3 by $O(100)$ in the log likelihood[1], which indicates the goodness-of-fit (Suyu et al. 2006) but in the meantime, the χ^2 of image position modeling worsens for S2, S4, and S5 by comparable amounts. Notably, this model can be considered as an additional test illustrating the significant differences in the predicted S0 mass when adding a third lens plane. However, the value of $\theta_{E,z=1.36} = 0.59''$ is lower than for typical dark-matter halos and the best-fit perturber centroid does not fall in the vicinity of HST-detected galaxies. This shows that the actual LoS structure in CSWA 31 is complex and cannot be fully captured by SIS profiles. Possible asymmetries in the overall group-scale mass distribution could also play a role.

5. Summary

In this work, we explore the constraints on the total masses of secondary lenses obtained from multi-plane strong lensing modeling. We perform a case study of a lensed spiral galaxy at

[1] After marginalizing over the source intensity pixel parameters; i.e., the log likelihood of the lens mass parameters is the log evidence of the source intensity reconstruction given the lens mass parameters

$z = 1.49$ in CSWA 31, which is along the LoS to the BGG and its group halo at $z = 0.683$. This system forms a rare, well-suited configuration with multiple image sets at different redshifts, providing tight constraints on the lens model, and adequate data to infer the maximum circular velocity of the spiral.

We measure the total mass of S0 from independent strong lensing and kinematic modeling, in order to assess the robustness of secondary lens mass measurements (see Sect. 4). Relying on the detailed strong lensing analysis of Wang et al. (2022), we measure the S0 mass with a range of models based on different constraints. We also model the velocity gradient using the least distorted image S0(d) with $\mu \simeq 7$, using the state-of-the-art software ^{3D}Barolo. We obtain a median $V_{\rm rot} = 123^{+117}_{-38.3}$ km s^{-1} at 3.3 kpc, consistent with other kinematic models of high-redshift disks of similar stellar masses (e.g., Genzel et al. 2017, 2020). The total mass of S0 is only compatible between the two approaches when adding a third lens plane to account for LoS perturbers.

We conclude that the secondary-lens measurement from the multiple-plane modeling includes high systematic uncertainties from degeneracies between lens planes and the complex LoS structure. Leveraging extended arcs as additional constraints can reduce the degeneracies. The secondary lens contributes less to the deflection angle of light from the source galaxies compared to the main lens, and its best-fit properties can easily be affected by other perturbers along the LoS, as they project their mass onto the secondary lens plane. Accounting for additional structures along the LoS is therefore key to improve the mass measurement of the secondary lens.

Acknowledgements

We thank E. Di Teodoro for helpful discussions and support on ^{3D}Barolo. HW, RC and SHS thank the Max Planck Society for support through the Max Planck Research Group and Max Planck Fellowship for SHS. AG acknowledges funding and support by the Swiss National Science Foundation (SNSF). C.G. acknowledges support through grant MIUR2020 SKSTHZ.

References

Auger, M. W., Treu, T., Bolton, A. S., et al. 2010, ApJ, 724, 511
Bayliss, M. B., Johnson, T., Gladders, M. D., Sharon, K., & Oguri, M. 2014, ApJ, 783, 41
Belokurov, V., Evans, N. W., Hewett, P. C., et al. 2009, MNRAS, 392, 104
Birrer, S., Treu, T., Rusu, C. E., et al. 2019, MNRAS, 484, 4726
Boquien, M., Burgarella, D., Roehlly, Y., et al. 2019, A&A, 622, A103
Bournaud, F., Elmegreen, B. G., & Martig, M. 2009, ApJ, 707, L1
Bradshaw, E. J., Almaini, O., Hartley, W. G., et al. 2013, MNRAS, 433, 194
Collett, T. E. 2015, ApJ, 811, 20
Di Teodoro, E. M. & Fraternali, F. 2015, MNRAS, 451, 3021
Di Teodoro, E. M., Grillo, C., Fraternali, F., et al. 2018, MNRAS, 476, 804
Gavazzi, R., Treu, T., Koopmans, L. V. E., et al. 2008, ApJ, 677, 1046
Genzel, R., Förster Schreiber, N. M., Übler, H., et al. 2017, Nature, 543, 397
Genzel, R., Price, S. H., Übler, H., et al. 2020, ApJ, 902, 98
Kennicutt, Robert C., J. 1998, ARA&A, 36, 189
Koopmans, L. V. E., Treu, T., Bolton, A. S., Burles, S., & Moustakas, L. A. 2006, ApJ, 649, 599
Mandelbaum, R., Eifler, T., Hložek, R., et al. 2018, The LSST Dark Energy Science Collaboration (DESC) Science Requirements Document
McGaugh, S. S. & Schombert, J. M. 2015, ApJ, 802, 18
Meneghetti, M., Natarajan, P., Coe, D., et al. 2017, MNRAS, 472, 3177
Nestor Shachar, A., Price, S. H., Förster Schreiber, N. M., et al. 2023, ApJ, 944, 78
Newman, S. F., Genzel, R., Förster-Schreiber, N. M., et al. 2012, ApJ, 761, 43
Peng, Y.-j., Lilly, S. J., Kovač, K., et al. 2010, ApJ, 721, 193
Popesso, P., Concas, A., Cresci, G., et al. 2023, MNRAS, 519, 1526
Price, S. H., Shimizu, T. T., Genzel, R., et al. 2021, ApJ, 922, 143

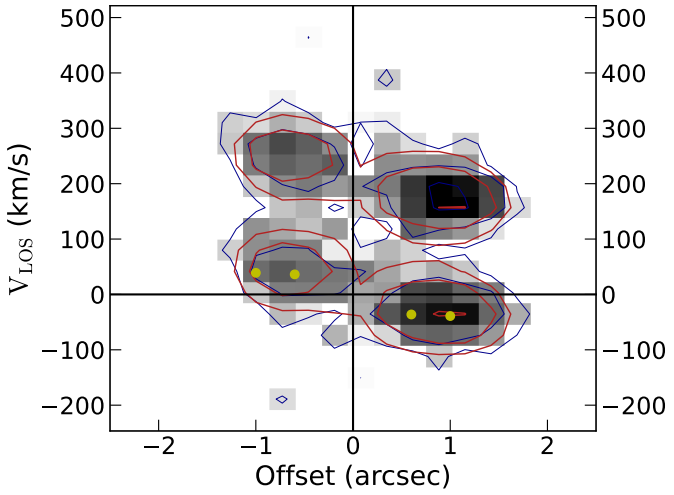

Fig. A.1: Position-velocity (PV) diagram along the major axis of S0(d) for the [OII] doublet. The contour levels and color coding are the same as Fig. 2. The yellow points show the position on the S0(d) image where we have secure velocity measurements. We set the $V_{\rm LoS} = 0$ km s^{-1} at the center of [OII]λ3726 Å emission line.

Puglisi, A., Dudzevičiūtė, U., Swinbank, M., et al. 2023, MNRAS, 524, 2814
Salpeter, E. E. 1955, ApJ, 121, 161
Schneider, P. 2014, arXiv e-prints, arXiv:1409.0015
Shajib, A. J., Vernardos, G., Collett, T. E., et al. 2022, arXiv e-prints, arXiv:2210.10790
Soto, K. T., Martin, C. L., Prescott, M. K. M., & Armus, L. 2012, ApJ, 757, 86
Stark, D. P., Auger, M., Belokurov, V., et al. 2013, MNRAS, 436, 1040
Suyu, S. H. & Halkola, A. 2010, A&A, 524, A94
Suyu, S. H., Hensel, S. W., McKean, J. P., et al. 2012, ApJ, 750, 10
Suyu, S. H., Marshall, P. J., Hobson, M. P., & Blandford, R. D. 2006, MNRAS, 371, 983
Swinbank, A. M., Papadopoulos, P. P., Cox, P., et al. 2011, ApJ, 742, 11
Treu, T. 2010, ARA&A, 48, 87
Übler, H., Genzel, R., Wisnioski, E., et al. 2019, ApJ, 880, 48
Wang, H., Cañameras, R., Caminha, G. B., et al. 2022, A&A, 668, A162
Wisnioski, E., Förster Schreiber, N. M., Wuyts, S., et al. 2015, ApJ, 799, 209
Wong, K. C., Suyu, S. H., Auger, M. W., et al. 2017, MNRAS, 465, 4895
Yu, S.-Y., Xu, D., Ho, L. C., Wang, J., & Kao, W.-B. 2022, A&A, 661, A98

Appendix A: Kinematics of S0

We present the kinematic modeling results from ^{3D}Barolo and the stellar-mass Tully-Fisher relation in Figs. A.1, A.2 and A.3.

Appendix B: Model Esr-3MP

We present the degeneracies of the mass parameters in model Esr-3MP in Fig. B.1.

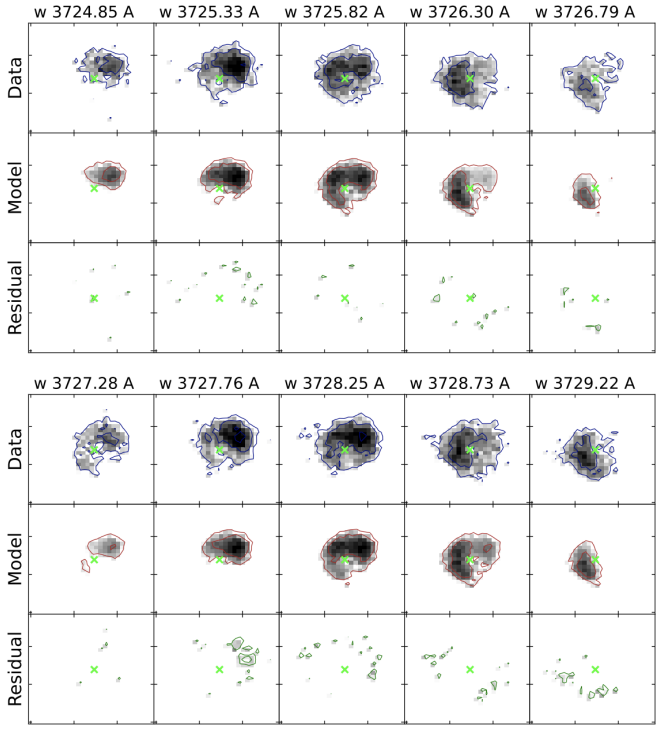

Fig. A.2: Channel maps for the kinematic models with 3 rings. The contour colors and levels are the same as the Fig. 2. The residual of the [OII]λ3729 Å emission line (bottom row) is worse than the models with 4 rings.

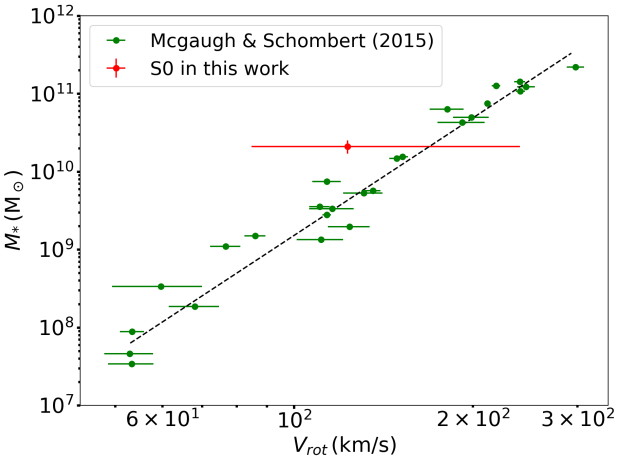

Fig. A.3: The stellar-mass Tully-Fisher relation. The green points show the sample of galaxies at $z \simeq 0$ from McGaugh & Schombert (2015) (their Tab. 7), and the dashed line shows the corresponding best-fitting relation. The red point shows the S0 spiral at $z = 1.49$ in this work with 1-σ uncertainty, which is consistent with the local Tully-Fisher relation.

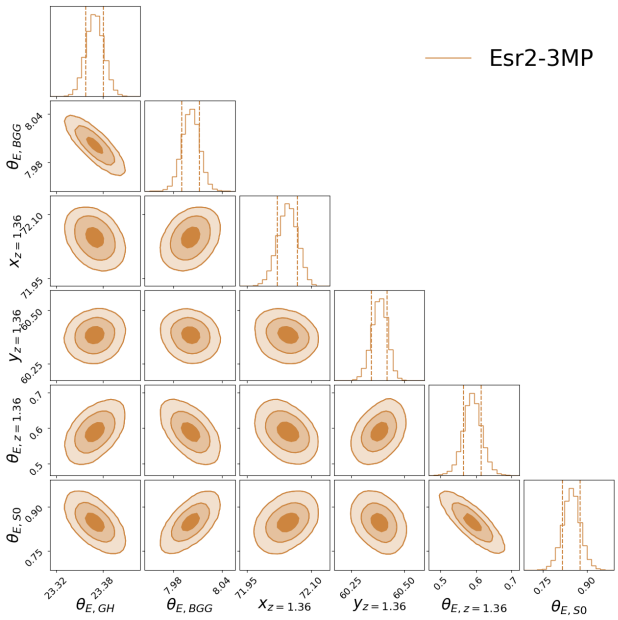

Fig. B.1: Joint posterior PDFs for the model Esr2-3MP based on two extended sources and image positions. We show the parameters presenting the lens masses at three multiple planes. The $\theta_{E,GH}$ and $\theta_{E,BGG}$ are the Einstein radius of the group halo and the BGG at the main lens plane at $z = 0.683$. The $x_{z=1.36}$ and $y_{z=1.36}$ are the centroid of the perturber and the $\theta_{E,z=1.36}$ is its Einstein radius. The $\theta_{E,S0}$ is the Einstein radius of S0 at $z = 1.49$. The three shaded areas on the joint PDFs show the 68.3%, 95.4%, and 99.7% credible regions. The 1D histograms show the marginalized PDFs for the selected mass parameters, and the vertical lines mark the 1σ confidence intervals. The $\theta_{E,S0}$ shows strong degeneracies with $\theta_{E,BGG}$, $\theta_{E,GH}$ and $\theta_{E,z=1.36}$.